# Absorption spectroscopy and Stokes polarimetry in a $^{87}$Rb vapour in the Voigt geometry with a 1.5 T external magnetic field

View the article online for updates and enhancements.

# Absorption spectroscopy and Stokes polarimetry in a $^{87}$Rb vapour in the Voigt geometry with a 1.5 T external magnetic field

**Francisco S Ponciano-Ojeda**[*] , **Fraser D Logue** and **Ifan G Hughes**

Joint Quantum Centre (JQC) Durham-Newcastle, Department of Physics, Durham University, South Road, Durham, DH1 3LE, United Kingdom

E-mail: francisco.s.ponciano-ojeda@durham.ac.uk

CrossMark

## Abstract
This paper provides details of a spectroscopic investigation of a thermal $^{87}$Rb atomic vapour. The experiment was conducted with an external magnetic field of 1.5 T in the Voigt geometry. Very good quantitative agreement between experimental data and theory is found for all four Stokes parameters—with RMS errors of $\sim 1.5\%$ in all cases. From the fits to our experimental data a value for the magnetic field strength is extracted, along with the angle between the magnetic field and the polarisation of the light. The effects of the cell window birefringence on the optical rotation signals are characterised. This allows us to carry out precise measurements at a high field strength and arbitrary geometries, allowing further development of possible areas of application for atomic magnetometers.

(Some figures may appear in colour only in the online journal)

## 1. Introduction

Over the past decades atomic spectroscopy has cemented itself as one of the cornerstones of precision measurements. From helping define the standards for time-keeping [1–3] to measurement of electromagnetic fields [4–9], spectroscopic techniques have become key tools in high precision systems. In recent years, together with the push for new technologies in other areas, this has seen the field of atom-based sensors burgeon. Of particular interest are magnetic field sensors [10] which rely on the interaction of the nuclear and elec-

tronic spins with the external field and well-known spectroscopic signals. Applications of such atomic sensors span a variety of disciplines, ranging from explosives detection [11]; microfluidics [12]; medical imaging of soft tissues [13–16]; gyroscopes [17]; and measurements on spin-active solid-state systems [18]. In order to improve and sustain the development of these technologies, atomic spectroscopy in the presence of external magnetic fields has become an area of wide interest [19–23]. This in turn has given rise to a variety of experiments and optical devices [24–31] that help demonstrate the depth of understanding of the physics involved in said interactions, furthering the reach and possible applications of this area. Nevertheless, this in-depth understanding of the interactions between atoms and an externally applied magnetic field has primarily occurred for fields up to $\sim 1$ T.

The use of spectroscopic techniques in atomic systems has received less attention at the higher end ($> 1$ T) of the range

---

[*] Author to whom any correspondence should be addressed.

of field strengths for different reasons. There is the matter of most methods used to obtain large fields being destructive in their nature, thus complicating the experimental reproducibility. In such experiments, the Zeeman splitting of energy levels in alkali-metal atoms is used to observe field strengths of the order of tens/hundreds of Tesla via spectroscopic techniques [32–34]. Non-destructive techniques for producing these large fields also exist, and this has enabled work in large pulsed magnetic fields up to 58 T with similar alkali-atom systems [35, 36]. Aside from the large Zeeman splitting produced at such large magnetic fields, there are other changes in the atoms that in turn allow additional effects to be observed. Of these changes the most relevant is the decoupling of the nuclear and electronic spins in the atom, with the external magnetic field now being a common axis for the precession of both. This is known as the hyperfine Paschen–Back (HPB) regime [37–43] and, in contrast to the experiments at lower fields ($< 10$ mT)—where it is easily and directly measured [10]—the Larmor precession frequency is not of interest as it can be too high for conventional electronic systems. Rather, the characteristic absorption spectrum of the atomic system is a more straightforward way of obtaining information about the magnetic field.

Work has previously been done in atomic vapours of both low and high atomic densities [44–46], and other relevant magneto-optic effects have been the subject of extensive studies [47–50]. This atom–light interaction while in the presence of an external magnetic field has also been used in other systems such as [21, 51–53]. For the majority of said work the $\vec{k}$ vector of the laser beam used is parallel to the direction of the external magnetic field $\vec{B}$—the Faraday geometry. This gives rise to characteristic absorption spectra that are highly symmetric [41, 54] and reflect only the magnitude of the magnetic field [42]. However, there has been some work [55, 56] that makes use of the less studied Voigt configuration where, rather than being parallel, the $\vec{k}$ vector of the light and the direction of the magnetic field $\vec{B}$ are perpendicular. The change in geometry results in a change in the atomic transitions permitted by the selection rules [57, 58] and thus allows for information not only on the magnitude but also on the direction of the magnetic field to be experimentally observed.

In this work we provide a detailed spectroscopic analysis of measurements taken in the Voigt geometry with an atomic vapour at a magnetic field strength of 1.5 T. These measurements include optical rotation signals, expressed in terms of the Stokes parameters. Our theoretical model *ElecSus* describes the atomic susceptibility [59, 60] and provides a means of fitting the experimental data, from which values of the magnetic field strength are extracted and compared against expected values. From the fit we also extract the relative orientation of the magnetic field to a given known input light polarisation. Finally, we demonstrate a method to measure the birefringence of the cell windows by looking at small changes in the expected optical rotation signals produced by the atomic medium in the presence of a strong external magnetic field.

The text continues in the following manner: section 2 gives a brief summary of the theory behind the model used in

analysing our experimental data; the experimental methods to obtain these data are presented in section 3; a discussion and comparison of our model and the experimental spectra appear in section 4. The paper finishes with further elaboration upon the analysis of our experimental data in section 5 where the optical rotation signals are used to extract information regarding the birefringence introduced by the cell windows.

## 2. Theoretical model

In order to fit our experimental data we use *ElecSus*. The theory behind this software has been treated in detail in references [59, 60]. For this work we summarise this theory and highlight the points of most relevance. We begin by assuming an atom–light system operating in the weak-probe regime [61, 62], although recent work [46] provides methods to generalise this into a strong-probe regime. The base for the model lies in using the complex electric susceptibility of the atomic medium, $\chi(\Delta)$, as a function of the optical frequency detuning $\hbar\Delta = (\hbar\omega_{\text{laser}} - \hbar\omega_0)$ near the alkali D-line resonances. Here we define $\omega_{\text{laser}}$ as the angular frequency of the laser and $\omega_0$ as the angular frequency of the atomic transition. We also note that experimentally it is more common to use linear detuning, $\Delta/2\pi$. Using a matrix representation we construct the atomic states for our system in the uncoupled $m_L, m_S, m_I$ basis. We can then account for the internal energy levels that come about as a result of the fine and hyperfine structure to which we add terms relevant in describing interactions with external magnetic fields, via the Zeeman effect. With this representation of the Hamiltonian for the atomic system, we proceed to calculate the eigenvalues, which correspond to the transition energies, and absolute line strengths from the dipole matrix elements. As a final step, we incorporate the Doppler effect in our model via a Voigt profile (convolution of the Lorentzian homogeneous linewidth and the Gaussian from the Maxwellian velocity distribution) for each of the atomic transitions as defined by their energy and strength. In this manner, the total susceptibility of the medium is calculated as the sum of the individual susceptibilities for all dipole-allowed transitions, each with an effective detuning in the scope of a global linear detuning. At this point it is convenient to split the susceptibility into separate components for $\sigma^{\pm}$ and $\pi$ transitions.

For a given total susceptibility the propagation of light through the atomic medium is done by solving the corresponding wave equation and finding the two propagation eigenmodes. Each eigenmode is expressed in terms of the components of the susceptibility, which allow the light to couple to the transitions in distinct ways. One can also find a relation between the eigenmodes and the complex refractive indices of the medium. The exact coupling of the eigenmodes to the transitions depends on the geometry of the atom–light system. In our experiment the system is set up in the Voigt geometry as shown in figure 1, which consists of setting the externally applied magnetic field vector $\vec{B}$ perpendicular to the light wavevector $\vec{k}$. We further constrain the geometry of the system by taking the electric field vector of our laser beam $\vec{E}$ along the Cartesian $x$-axis, which allows us to consider our
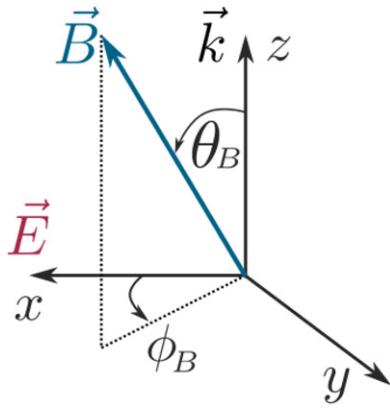
**Figure 1.** General geometry for experiments involving an externally applied magnetic field and light; for the Voigt geometry where $\vec{k} \perp \vec{B}$, $\theta_B = \pi/2$. The light is assumed to be linearly polarised in the $x - y$ plane, with the electric field vector $\vec{E}$ taken here to be vertically polarised along the $x$-axis. The external magnetic field $\vec{B}$ makes an angle $\phi_B$ with respect to $\vec{E}$, which when projected onto the $x - y$ plane gives components parallel and perpendicular to $\vec{E}$. The former drives $\pi$ transitions and the latter $\sigma^\pm$ transitions.

beam as a linearly polarised plane-wave propagating along the $z$-axis and polarised in the $x - y$ plane. In this manner, for the Voigt geometry we take the external magnetic field vector in the $x - y$ plane, with an angle $\phi_B$ defined as the direction of said vector relative to the $x$-axis ($\vec{E}$). This angle also gives a simple way of describing the relative coupling of the light to the atomic electron transitions as a consequence of the projections of $\vec{B}$ onto $\vec{E}$, which in turn change the angular-momentum algebra. For a projection of $\vec{B}$ parallel to the polarisation of the light (i.e. $\vec{E}$) $\pi$ transitions with $\Delta m_J = 0$ are driven, while for a projection of $\vec{B}$ perpendicular to the polarisation of the light the $\sigma^\pm$ transitions, with $\Delta m_J = \pm 1$, are driven [63]. Circular polarisation of left- or right-handedness in the Voigt geometry can be treated by assuming a linear combination of the $x$ and $y$ components of linearly polarised light as there is no immediate effect of the relative phase between the two. In this particular case, the relative phase $\phi = (2n - 1)\pi/4$, with $n$ an integer, is merely reflected in the strength of each component, which is equal for the $x$ and $y$ components. A corollary of the above is that the system exhibits equivalent solutions for values of $\phi_B$ modulo $\pi$, and this in turn results in the inability to determine the absolute direction of the magnetic field with just one measurement.

As mentioned above, the propagation through the atomic medium of each of the eigenmodes has an associated complex refractive index. In general, the medium has two unique refractive indices, which in light of them being complex, gives rise to dichroism and birefringence. To take these effects into account, the electric field of the light is propagated through the atomic medium. The input electric field is first transformed into the coordinate system of the medium's eigenbasis, which corresponds to the Cartesian basis in the Voigt geometry, with the orthogonal components coinciding with the parallel and perpendicular directions to the external magnetic field vector. Once the field has been written in this new basis it is propagated using each index, $n_i$, over a distance $L$ in the medium by

using the multiplicative factor $e^{i n_i k L}$. The resulting electric field is then transformed back into the laboratory coordinate system. At this stage the output electric field can be conveniently analysed via Stokes polarimetry [50, 64]. This formalism provides a set of parameters which are easily obtained with standard laboratory equipment and measurements of the intensity of light in different sets of orthogonal polarisation bases. The Stokes parameter $S_0$ is independent of the measurement basis, and for an incident beam of intensity $I_0$ is defined as

$$S_0 \equiv \frac{I_x + I_y}{I_0} = \frac{I_\nearrow + I_\searrow}{I_0} = \frac{I_{\text{RCP}} + I_{\text{LCP}}}{I_0}. \tag{1}$$

Physically, $S_0$ represents the normalised total transmitted intensity. The remaining Stokes parameters, $S_1$, $S_2$ and $S_3$,

$$S_1 \equiv \frac{I_x - I_y}{I_0}, \tag{2}$$

$$S_2 \equiv \frac{I_\nearrow - I_\searrow}{I_0}, \tag{3}$$

$$S_3 \equiv \frac{I_{\text{RCP}} - I_{\text{LCP}}}{I_0}, \tag{4}$$

give information on the optical rotation of light generated by the atomic medium by looking at the differences between the orthogonal polarisation components in the horizontal ($I_x$, $I_y$), diagonal ($I_\nearrow$, $I_\searrow$) and circular bases ($I_{\text{RCP}}$, $I_{\text{LCP}}$), respectively.

## 3. Experimental setup

Experimental work for this paper was carried out using the optical setup described in figure 2. The laser used is a tuneable distributed feedback (DFB) laser, with a central wavelength of 780 nm and a quoted linewidth of $< 2$ MHz. The frequency is tuned by changing the temperature of the laser chip, which allows a frequency mode-hop free tuning range over many hundreds of GHz. A typical scan of this size takes $\sim 2$ s and is limited by the response time of the temperature control circuit of the laser. The emitted light from the laser is split using polarisation optics after an optical isolator (OI) to maintain high polarisation purity and manage the beam intensity. Some of the light is taken to a secondary optical setup for calibration of the laser frequency scan. A signal from a 75 mm natural abundance Rb reference cell provides an absolute frequency reference, whereas a transmission signal from a Fabry–Pérot etalon is used to linearise the scan. These two signals are then processed as outlined in reference [67] to obtain spectra as a function of linear detuning. The remainder of the light is then passed through several polarising elements that allow us to obtain a well-defined linear polarisation to use in our experiment cell. A circular polarisation can be obtained by replacing the half-wave retarder plate ($\lambda/2$) for a quarter-wave retarder plate ($\lambda/4$) before the light goes through the experiment cell.

The experiments are carried out in a cuboidal vapour cell with a cavity length of 1 mm containing isotopically enriched 99% purity $^{87}$Rb. In order to provide a large enough atomic density and optical depth for observing the desired phenomena
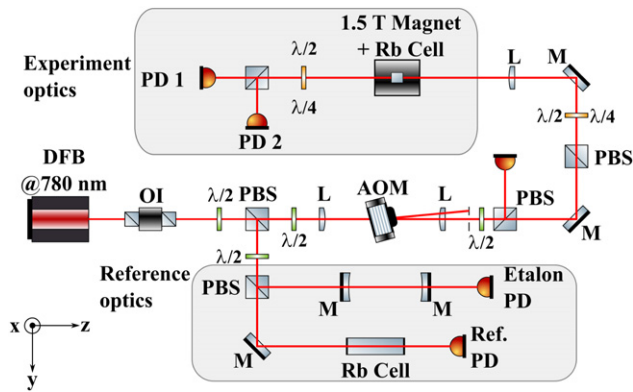
**Figure 2.** Schematic of the most relevant components of the optical setup used for acquiring experimental data. Light from a DFB laser passes through an OI and is split into two components. Approximately half of the light is used for a reference optical system used to calibrate the laser scan in a zero magnetic field environment; the system consists of a room temperature 75 mm natural abundance Rb reference cell and a Fabry–Pérot etalon made with two mirrors (M). The rest of the light is sent to the experiment cell via an acousto-optic modulator that can be used to keep the power constant [65] and polarising beamsplitter (PBS) cubes and half-/quarter-wave plates ($\lambda/2$ and $\lambda/4$, respectively) to ensure the input light is in the desired polarisation state. The 1 mm long experiment cell contains isotopically enriched $^{87}$Rb (99% purity), and is placed in a cylindrical magnet designed to give a primarily axial field of 1.62 T at its centre [66]. A polarisation-sensitive detection scheme is used after the experiment cell, consisting of a PBS, retarder wave plate and two balanced photodiodes (PD), that allow a voltage signal with information on the optical rotation and absorption of the medium to be measured. Plano-convex lenses (L) are used to resize the beam at different points in order to avoid significant clipping.

the cell must be heated. Microfabricated cells, such as this one, have previously been found to exhibit birefringent properties when heated to their optimal operating temperatures [68–71]. Details on the fabrication of this cell can be found in [72]. The cell and beam-steering optics (uncoated right-angle prisms) are placed in a custom-made copper holder which also houses an internal heater, as seen in figure 3. During operation the temperature is set by applying a voltage to the heater to raise the temperature of the copper surrounding the cell. The stability of the holder is maintained passively by fixing the voltage and allowing thermalisation of the metal block with the surroundings. The copper bed is enclosed in a secondary cylinder made of PTFE that acts as a shield and is only in weak thermal contact with it in order to ensure there are no sharp fluctuations in the temperature of the system. Due to the reduced footprint of the system imposed by the central bore size of the magnet it was not possible to include a suitable temperature sensor in this mount.

The external magnetic field is generated by a cylindrical permanent magnet, with a central bore of diameter 22 mm along its axis, designed using the 'magic sphere' configuration described in [66]. The maximum value of the field produced by the magnet is 1.62 T at its centre, with the field strength quickly falling radially outwards to the ends of the magnet. The cylindrical PTFE assembly housing the copper heater block with the experiment cell sits inside the magnet's bore. This
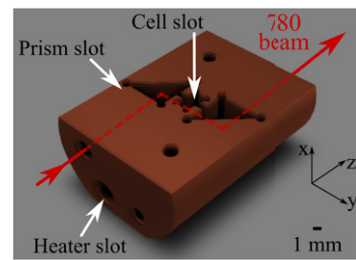


**Figure 3.** Internal copper heater block used in the experiments in the Voigt geometry. Shown here is the main copper block, with an angled slot for the 1 mm cell to avoid back-reflection from the cell windows and two spaces for 5 mm right-angle prisms. Light enters and exits the heater block through two optical access holes (seen in the upper-left) and passes through the cell perpendicular to its original direction of incidence. The larger hole (bottom-centre) houses a resistive heater element that serves to heat the entire block in order to raise the temperature of the vapour in the interior of the cell to the desired point. This block is covered by a copper lid and housed in a custom PTFE cylinder that preserves the optical access and cable feed-throughs necessary to carry out experiments when the whole assembly is located inside the permanent magnet.

particular design allows for a well-characterised field along the axis of the magnet, which in turn ensures field homogeneity across the length of the experiment cell, while maintaining the field on the outside of the magnet to below hundreds of mT. Further details on the construction and characterisation of the magnet can be found in reference [66].

The experiment is conducted in the weak-probe regime [62] to avoid optical pumping. Therefore the optical power of the interrogating laser beam (i.e. the probe beam) is maintained below the saturation intensity. For a beam waist ($1/e^2$) of approximately 0.7 mm this means keeping the power close to 1 $\mu$W. A probe beam of these characteristics gives an effective spatial resolution roughly equal to the volume of atoms interrogated by the laser beam, which can be considered to be a cylinder whose length is that of the experiment vapour cell (1 mm) and whose radius is the beam waist. It is worth nothing that the length of the cylindrical heater block assembly previously described (28 mm) is smaller than the length of the magnet (152 mm) and this generates difficulties in aligning the heater block axis relative to the laboratory frame of reference once inside the magnet. As such, the heater block is slightly rolled about the axis of the magnet ($z$) which in turn results in a relative orientation of the $x, y$ axes of the atom and the laboratory $x, y$ axes that can be described by an effective offset in the angle $\phi_B$.

## 4. Analysis of atomic absorption spectra at high fields

Figure 4 is created using the theoretical model described in section 2 and shows the evolution of the atomic energy levels as a function of magnetic field strength. In addition, the predicted absorption spectra in a 1.5 T external magnetic field are depicted. In the lower panel the ground- and excited-state energy level diagrams show, respectively, the states in the $5S_{1/2}$ and $5P_{3/2}$ manifolds at 1.5 T as well as the initial and final
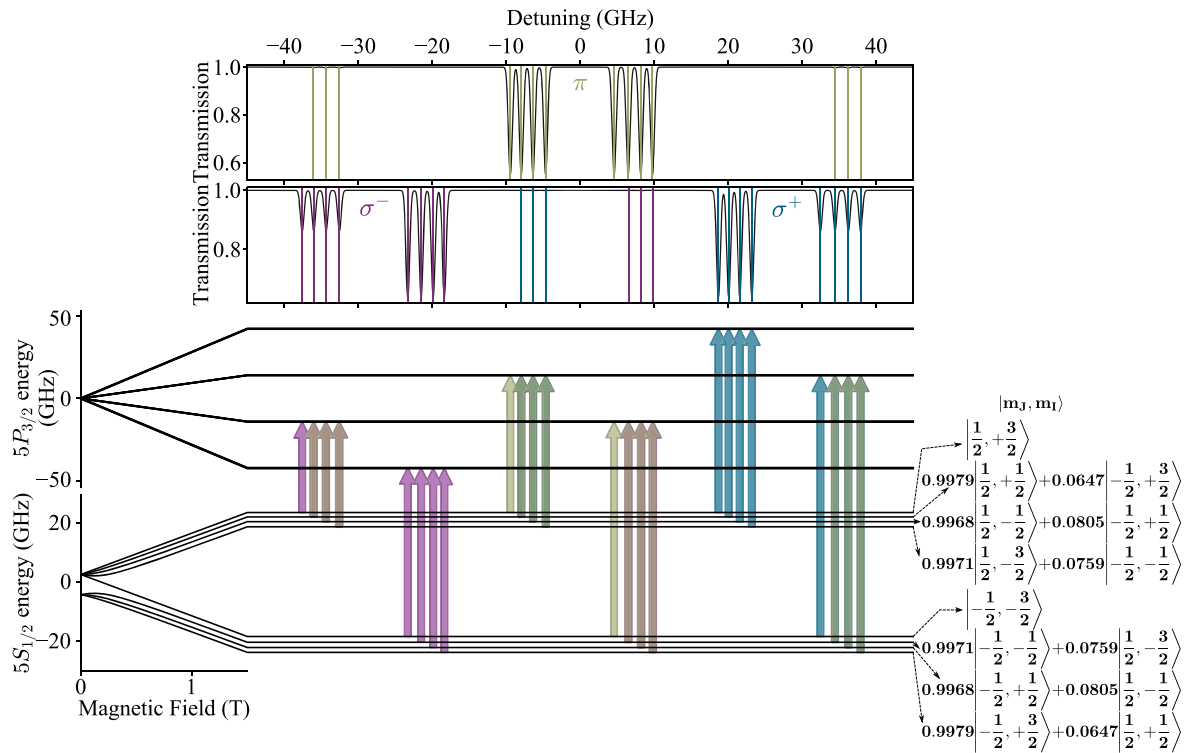
**Figure 4.** Spectroscopy of the Rb D$_2$ line for a system with an external magnetic field of 1.5 T arranged in the Voigt geometry. The bottom-left of the figure shows the evolution of the ground and excited state energy levels in $^{87}$Rb, corresponding to the $5S_{1/2}$ and $5P_{3/2}$ atomic energy levels, respectively, with an increasing magnetic field strength of up to 1.5 T. In the lower right of the figure, the ground-state levels involved in the atomic transitions at 1.5 T, including the admixtures due to remnant effects of the hyperfine interaction, are given in the $|m_J, m_I\rangle$ basis. The upper panels show the calculated spectra, as functions of linear detuning, for $\pi$ (olive) transitions ($\vec{E}\|\vec{B}$), and $\sigma^+$ (blue), $\sigma^-$ (purple) transitions ($\vec{E}\perp\vec{B}$). The coloured arrows in the energy level diagram point from the initial to the final states involved in the transition, with overlapping arrows showing the presence of weaker transitions due to the admixtures present in the system.

states involved in each of the allowed transitions. Seen in the top two panels are the calculated absorption for an isotopically enriched vapour cell (99% purity $^{87}$Rb) at 100°C, separated into $\pi$ (upper panel) and $\sigma^{\pm}$ (lower panel) transitions. The position of the vertical lines serves to indicate the atomic resonances in terms of the linear frequency. The colour of these lines corresponds to different types of transitions: $\pi$ transitions are olive green, $\sigma^+$ transitions are blue and $\sigma^-$ transitions are purple. For the ground state, the decompositions in the $m_J, m_I$ basis are given to the right of the corresponding sublevel. The arrows, with colours again corresponding to the type of transition as previously mentioned, are semi-transparent to evidence the fact there are still some overlapping transitions due to a small remnant admixture in the state decomposition due to hyperfine interactions. This can also be seen in the respective detunings of the transitions on the top two panels, where $\pi$ and $\sigma^{\pm}$ have frequencies that coincide between them.

At a field strength of 1.5 T, the $5P_{3/2}$ states strongly decouple into the $m_J, m_I$ basis and result in four multiplets organised by $m_J = 3/2, 1/2, -1/2, -3/2$ projections. Furthermore, at this magnetic field strength the ground state has a much more complete decoupling than that observed at lower field strengths [21, 42, 51–53, 56]. As such, we can treat the system as being completely in the HPB regime. This means that the initial hyperfine ground states are now split into two distinct groups, corresponding to the projections $m_J = \pm 1/2$, with the

$m_I = 3/2, 1/2, -1/2, -3/2$ states clearly defined despite the Doppler-broadening in the vapour. This gives us well-defined multiplets of four 'strong' transitions ($|m_J, m_I\rangle \rightarrow |m'_J, m_I\rangle$, with $m'_J = m_J(\pi), m_J + 1(\sigma^+), m_J - 1(\sigma^-)$). It is worth adding that at this point there are still some 'weak' transitions present due to the ground states not being pure eigenstates in the $m_J, m_I$ basis. This is evident in the small ($< 1\%$) admixture of the opposite $m_J$ state in the state decomposition on the bottom right of figure 4 (more details can be found in reference [42]).

Figures 5 and 6 show experimental data, averaged over five spectra, that have been fitted using the theory obtained with *ElecSus*. From the fit, the RMS error between data and theory is calculated for figure 5 and 6 to be 1.2%. The residuals $R$, multiplied by a factor of 100 for ease of viewing, are also shown. The absence of obvious structure in the residuals, and the large multiplier required for the residuals, are indicators of a very good fit [73]. The fit is carried out with three free parameters: $\phi_B$, the angle between the magnetic field and the direction of polarisation of the laser beam (see figure 1), taken to be linear along the $x(y)$-axis; $B$, the magnitude of the magnetic field the atoms are exposed to and $T$, the temperature of the atoms in the experiment cell. Other significant experimental parameters, such as those relating to the effects due to buffer gas in the cell, such as the amount of inhomogeneous broadening $\Gamma_{\text{Buff}}$ caused by collisions and a shift in the frequency of

J. Phys. B: At. Mol. Opt. Phys. **54** (2021) 015401
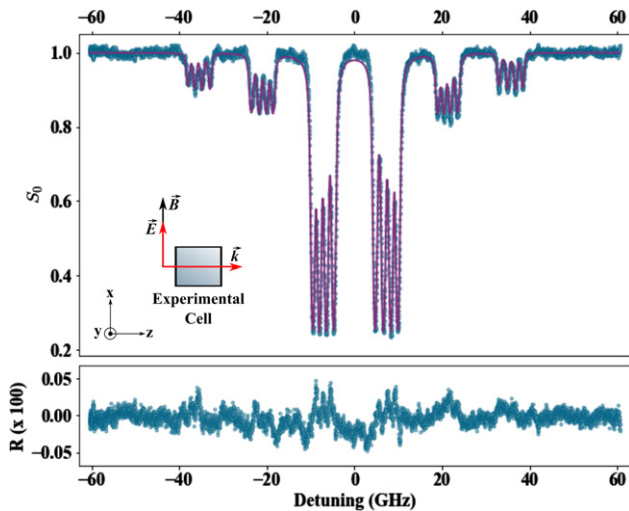
F S Ponciano-Ojeda *et al*



**Figure 5.** Experimental data (blue circles) expressed in terms of the linear detuning of the laser scan for a horizontally polarised input beam with the corresponding fit (purple line) using our *ElecSus* model, with residuals shown (bottom panel). Data and the theoretical fit are in very good agreement (RMS error of 1.2%). For this spectrum the free parameters in the fit are: $\phi_B$, the angle of the magnetic field with respect to the *x*-axis, $B$, the magnetic field strength and $T$, the temperature of the atoms. Average values of $\phi_B = (0.4491 \pm 0.0007)$ rad, $B = (1.52 \pm 0.08)$ T and $T = (108.94 \pm 0.04)$°C are obtained from fitting five spectra. All other parameters for the system are fixed as follows: $\theta_B = \pi/2$, $\Gamma_{\text{Buff}} = 350$ MHz and $\delta_{\text{shift}} = 50$ MHz.



**Figure 6.** Experimental data (blue circles) expressed in terms of the linear detuning of the laser scan for a vertically polarised input beam with the corresponding fit (purple line) using our *ElecSus* model, with residuals shown (bottom panel). Data and the theoretical fit are in very good agreement (RMS error of 1.2%). For this spectrum the free parameters in the fit are: $\phi_B$, the angle of the magnetic field with respect to the *x*-axis, $B$, the magnetic field strength and $T$, the temperature of the atoms. Average values of $\phi_B = (2.0082 \pm 0.0007)$ rad, $B = (1.52 \pm 0.07)$ T and $T = (110.23 \pm 0.03)$ C are obtained from fitting five spectra. All other parameters for the system are fixed as follows: $\theta_B = \pi/2$, $\Gamma_{\text{Buff}} = 350$ MHz and $\delta_{\text{shift}} = 50$ MHz.

the transitions $\delta_{\text{shift}}$, are kept fixed. The values for these fixed parameters are obtained *a priori* by fitting other spectra similar to those averaged and shown in figures 5 and 6. Of the remaining parameters in the fit, the field angle $\theta_B$ is fixed by the geometry of the experimental setup in the Voigt geometry ($\theta_B = \pi/2$). We attribute the significant buffer gas broadening in the spectra to He atoms trapped in the cell, after the cell was exposed to a He environment in previous experiments and note that this does not generate important shifts in any of the resonance lines. Using the literature values of the broadening coefficient for He [74], we extract a pressure of $\sim 18$ torr ($\sim 24$ mbar) for the amount of said buffer gas in our experiment cell. Note that while the time necessary to acquire a spectrum is on the order of a second, the time needed to analyse the data and generate a fit is on the order of minutes due to the complexity of the parameter space.

For the spectrum shown in figure 5 we obtain a value of $\phi_B = (0.4491 \pm 0.0007)$ radians ($(25.74 \pm 0.04)$°). Similarly, for the fit shown in figure 6 we obtain a value of $\phi_B = (2.0081 \pm 0.0007)$ radians ($(115.05 \pm 0.04)$°). Both of these values differ from their corresponding expected values by $\approx 0.45$ radians ($\sim 25$°), which we take as a systematic error due to the orientation of the cell heater block inside the bore of the cylindrical magnet used in the experiment. As a result, there is excitation of both $\pi$ and $\sigma^\pm$ transitions in both spectra shown due to the presence of parallel and perpendicular components of $\vec{B}$ along the direction of polarisation of the light. In this case, the difference in strength between the transitions is given as a simple factor of $\cos^2(\phi_B)$ for the
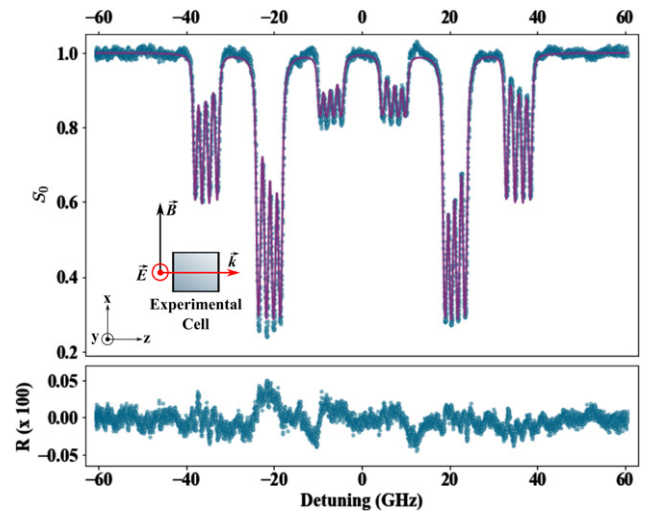
parallel component and $\sin^2(\phi_B)$ for the perpendicular component. According to the difference in the expected value of $\phi_B$ obtained from the fits, this results in an approximate 4 : 1 ratio in the strengths of the lines; this is clearly visible in both figures 5 and 6.

Similarly, for both spectra shown in figures 5 and 6 we obtain a value $B = 1.52$ T. The uncertainties in these values, 80 mT and 70 mT, respectively for the two spectra, can be mainly attributed to linearity of the laser scan in our experiment. The DFB laser used in our experiment allows for a large mode-hop-free scan ($\sim 150$ GHz) at the expense of a non-linearity that is introduced as the frequency is changed. It is this non-linearity, along with other systematic errors in the linearisation and calibration of the frequency axis, that is the primary source of uncertainty in our measurements. In future work we plan to design the experiment so that this non-linearity can be reduced in order to improve the precision in our measurement of the magnetic field strength.

Furthering the ideas and work presented in [56], we propose this as an atomic technique for measuring large magnetic fields and their relative orientation. With the system completely in the HPB regime, the Zeeman shift presented in all the resonance line positions allows for a better determination of the magnetic field strength. In addition to this, the relative strength between sets of transitions, due to different coupling strengths, is better observed. This in turn allows a more precise determination of the relative orientation of the direction of polarisation (i.e. of the electric field vector) of the light with respect to the external magnetic field. Thus, the present
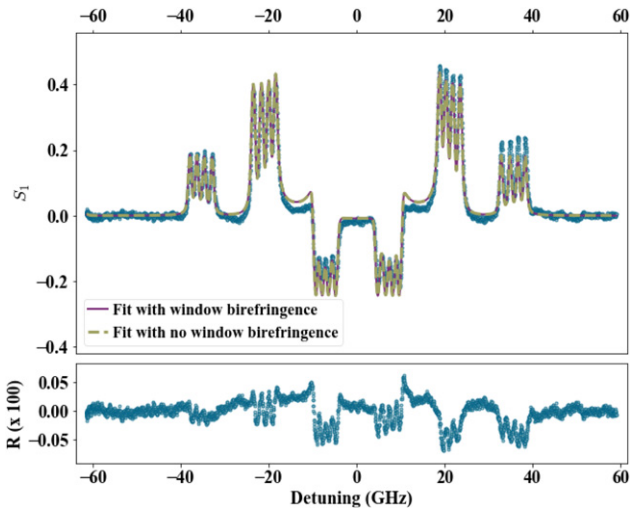
**Figure 7.** Experimental data (blue circles) taken as a function of linear detuning for a linearly polarised input beam with the corresponding fit (purple line) of the $S_1$ parameter taking window birefringence into account, with residuals $R$ shown. Data and the theoretical fit are in very good agreement (RMS error of ~2%). In this case the fixed parameters are $\Gamma_{\text{Buff}} = 350$ MHz, $\delta_{\text{shift}} = 50$ MHz and $\theta_B = \pi/2$, while the fit allows $T, B, \phi_B$ to float; also included in the fit are the parameters to take into account the birefringence effects of the cell windows ($\theta_{\text{BR}}, \phi_{\text{BR}}$). A fit without the effect of the cell window birefringence (broken line) is included for comparison.

**Figure 8.** Experimental data (blue circles) taken as a function of linear detuning for a linearly polarised input beam with the corresponding fit (purple line) of the $S_2$ parameter taking window birefringence into account, with residuals $R$ shown. Data and the theoretical fit are in very good agreement (RMS error of ~3%). In this case the fixed parameters are $\Gamma_{\text{Buff}} = 350$ MHz, $\delta_{\text{shift}} = 50$ MHz and $\theta_B = \pi/2$, while the fit allows $T, B, \phi_B$ to float; also included in the fit are the parameters to take into account the birefringence effects of the cell windows ($\theta_{\text{BR}}, \phi_{\text{BR}}$). A fit without the effect of the cell window birefringence (broken line) is included for comparison.

system and technique lead to a natural application of atomic-based spectroscopy in vector magnetometry.

## 5. Sensitivity of optical rotation signals to the birefringence of cell windows

At the high magnetic field strength used for this work, optical rotation phenomena can provide additional information about the medium through which the light propagates [75]. In the case of an atomic medium, measuring this optical rotation via the Stokes parameters, as mentioned in section 2, proves to be of natural interest for understanding the interactions between the atoms and the external magnetic field. In this case, we have experimentally measured the dichroism and birefringence of the atomic medium in the three bases corresponding to the $S_1, S_2$ and $S_3$ parameters as shown in figures 7–9, respectively.

In order to carry out these measurements a set of polarising optics (PBS $+\lambda/2$, $\lambda/4$) and two PD was set up, as seen in figure 2, to measure the light transmitted through the experiment cell in terms of the linear detuning of the laser scan. This allows for two orthogonal polarisation components to be recorded simultaneously and then be processed into the corresponding Stokes parameter for the basis in question. We take the definitions of the Stokes parameters as used in references [59, 60]. Figure 7 shows the $S_1$ parameter, taken as the difference between the orthogonal linear polarisations (i.e. horizontal and vertical) (equation (2)). Figure 8 shows the $S_2$ parameter, defined as the difference between the linear polarisations in a basis rotated by $\pi/4$, giving diagonal components in a Cartesian basis (equation (3)). Lastly, figure 9 shows the
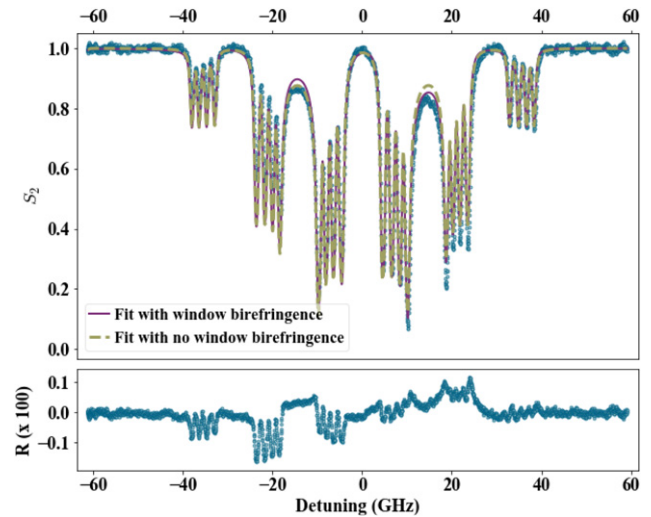
last Stokes parameter, $S_3$, as the difference between orthogonal circular polarisations in the helicity basis, (i.e. left-hand and right-hand circular) (equation (4)). In these cases, given a well-defined input polarisation, the transmitted light gives information regarding the linear and circular birefringence of the atomic medium.

Using our theoretical model, *ElecSus*, we proceed to fit the data to each of the three Stokes parameters mentioned above. Very good agreement [73] between the model (solid purple curve) and data (blue circles) is evident in figures 7–9. Despite this, there are still slight discrepancies between the experimental data and the fit. We can try and remove some of these errors by taking into account the birefringence of the windows of our experiment cell. To do this, we include in our model the effects of two thin, birefringent windows interacting with the electric field of our laser beam twice: once before the light enters the atomic medium and once when the light has passed through the atomic medium and exits the cell. We carry out these calculations by using the Jones matrix formalism [60], so that in this case the transmitted electric field $E_{\text{out}}$ in our experiment can be written as

$$E_{\text{out}} = \mathcal{M}_{\theta_{\text{BR}}, \phi_{\text{BR}}} \times \mathcal{J}_{\text{atoms}} \times \mathcal{M}_{\theta_{\text{BR}}, \phi_{\text{BR}}} \times E_{\text{in}},$$

where $E_{\text{in}}$ is the incident electric field, $\mathcal{M}_{\theta_{\text{BR}}, \phi_{\text{BR}}}$ is the Jones matrix representing the birefringent window of the cell and $\mathcal{J}_{\text{atoms}}$ is the Jones matrix representing the dichroic and birefringent atomic medium. The matrix $\mathcal{M}_{\theta_{\text{BR}}, \phi_{\text{BR}}}$ has been included twice to account for the entry and exit windows of the experiment cell. This output electric field can be multiplied by the appropriate Jones' matrices to give the desired polarisation
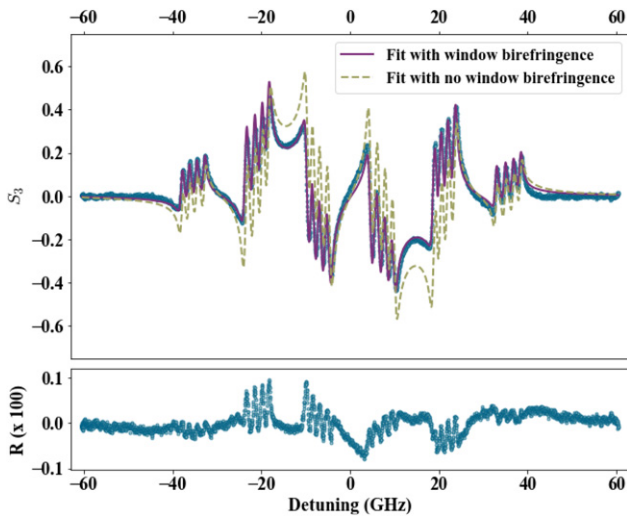
**Figure 9.** Experimental data (blue circles) taken as a function of linear detuning for a linearly polarised input beam with the corresponding fit (purple line) of the $S_3$ parameter taking window birefringence into account, with residuals $R$ shown. Data and the theoretical fit are in very good agreement (RMS error of $\sim$2%). In this case the fixed parameters are $\Gamma_{\text{Buff}} = 350$ MHz, $\delta_{\text{shift}} = 50$ MHz and $\theta_B = \pi/2$, while the fit allows $T, B, \phi_B$ to float; also included in the fit are the parameters to take into account the birefringence effects of the cell windows ($\theta_{\text{BR}}, \phi_{\text{BR}}$). A fit without the effect of the cell window birefringence (broken line) is included for comparison.

components to process into the form of the different Stokes' parameters.

From our fits we can see that the birefringence due to the cell windows is considerably small. In this case the cell windows have a thickness of 300 $\mu$m each [72]. Using the literature value for the Verdet coefficient of glass [76] at the wavelength of the Rb D$_2$ line ($\sim$ 780 nm), each cell window induces a rotation of $\approx 0.05°$. Here we make an initial assumption that both of these windows are identical in their birefringent properties. Figures 7–9 show very good agreement between the data (blue circles) and the model considering birefringence (broken green curve) [73]. The residuals $R$ shown in these figures correspond to the results of the fits that include the birefringence of both cell windows. We obtain average values of $(0.96 \pm 0.16)$ radians $((55 \pm 9)°)$ for the angle $\theta_{\text{BR}}$ and of $(0.06 \pm 0.03)$ radians $((3 \pm 2)°)$ for the angle $\phi_{\text{BR}}$. It is worth noting that these values correspond to a fit of the effect *both* cell windows have on the electric field transmitted through the cell. Comparing the fits to the experimental data with and without the birefringence effects from the cell windows we can see that this effect is particularly evident in the $S_3$ parameter, as seen in figure 9. Due to the definition of said parameter (equation (4)) we can proceed to say that the cell windows have a predominantly circular birefringence. The discrepancy between the rotation induced in the cell due to the field ($\approx 0.1°$) and the measured value for $\phi_{\text{BR}}$ is assumed to be caused by the heating of the windows as well as mechanical stresses from the fabrication process and the optical setup. In particular, we exploit the sensitivity of the atomic system to optical rotation, in this case in the basis of orthogonal circular polarisation states, to obtain a signal that enhances these effects so that they are

clearly visible. As such, this experimental system provides a tool to characterise these birefringence effects due to vapour cell windows in order to reduce systematic errors in future measurements.

## 6. Conclusions

In this work we have presented a spectroscopy-based technique using a thermal alkali-metal vapour that allows absolute magnetic field strength and orientation of the field with respect to the light polarisation to be measured. An isotopically enriched sample of $^{87}$Rb was used; however the principles behind this technique can be easily applied to other alkali-metal atoms. Very good agreement was found between the theoretical model used and our detailed spectroscopic measurements of the Stokes parameters of the medium. We have used polarisation-sensitive detection in order to better constrain the polarisation angle measured, as well as measure the birefringence effects due to the vapour cell windows. Using this technique it is also possible to envisage a precise spectroscopy setup for atomic magnetometry in large ($> 1$ T) fields. Furthermore, the work here presented opens up new areas of research using atomic vapours, such as measurement of fundamental constants via precision thermometry using the ground-state populations.

## ORCID iDs

Francisco S Ponciano-Ojeda ⬤ https://orcid.org/0000-0002-2090-7385
Fraser D Logue ⬤ https://orcid.org/0000-0001-7657-6135

## References

[1] Terrien J 1968 News from the international bureau of weights and measures *Metrologia* **4** 41
[2] Campbell G K and Phillips W D 2011 Ultracold atoms and precise time standards *Phil. Trans. R. Soc.* A **369** 4078
[3] Ludlow A D, Boyd M M, Ye J, Peik E and Schmidt P O 2015 Optical atomic clocks *Rev. Mod. Phys.* **87** 637
[4] Osterwalder A and Merkt F 1999 Using high Rydberg states as electric field sensors *Phys. Rev. Lett.* **82** 1831
[5] Thiele T, Deiglmayr J, Stammeier M, Agner J A, Schmutz H, Merkt F and Wallraff A 2015 *Phys. Rev.* A **92** 063425

J. Phys. B: At. Mol. Opt. Phys. **54** (2021) 015401

F S Ponciano-Ojeda *et al*

[6] Sedlacek J A, Schwettmann A, Kübler H and Shaffer J P 2013 Atom-based vector microwave electrometry using rubidium Rydberg atoms in a vapor cell *Phys. Rev. Lett.* **111** 063001

[7] Kumar S, Fan H, Kübler H, Sheng J and Shaffer J P 2017 Atom-based sensing of weak radio frequency electric fields using homodyne readout *Sci. Rep.* **7** 1

[8] Horsley A, Du G-X and Treutlein P 2015 Widefield microwave imaging in alkali vapor cells with sub-100 $\mu$m resolution *New J. Phys.* **17** 112002

[9] Horsley A and Treutlein P 2016 Frequency-tunable microwave field detection in an atomic vapor cell *Appl. Phys. Lett.* **108** 211102

[10] Budker D and Romalis M 2007 Optical magnetometry *Nat. Phys.* **3** 227

[11] Lee S K, Sauer K L, Seltzer S J, Alem O and Romalis M V 2006 Subfemtotesla radio-frequency atomic magnetometer for detection of nuclear quadrupole resonance *Appl. Phys. Lett.* **89** 2004

[12] Xu S, Crawford C W, Rochester S, Yashchuk V, Budker D and Pines A 2008 *Phys. Rev.* A **78** 013404

[13] Bison G, Castagna N, Hofer A, Knowles P, Schenker J-L, Kasprzak M, Saudan H and Weis A 2009 A room temperature 19-channel magnetic field mapping device for cardiac signals *Appl. Phys. Lett.* **95** 173701

[14] Alem O *et al* 2015 Fetal magnetocardiography measurements with an array of microfabricated optically pumped magnetometers *Phys. Med. Biol.* **60** 4797

[15] Sander T H, Preusser J, Mhaskar R, Kitching J, Trahms L and Knappe S 2012 Magnetoencephalography with a chip-scale atomic magnetometer *Biomed. Opt. Express* **3** 981

[16] Boto E *et al* 2017 A new generation of magnetoencephalography: room temperature measurements using optically-pumped magnetometers *Neuroimage* **149** 404

[17] Donley E A, Long J L, Liebisch T C, Hodby E R, Fisher T A and Kitching J 2009 *Phys. Rev.* A **79** 013420

[18] Arnold D, Siegel S, Grisanti E, Wrachtrup J and Gerhardt I 2017 A rubidium $M_x$-magnetometer for measurements on solid state spins *Rev. Sci. Instrum.* **88** 023103

[19] Sargsyan A, Tonoyan A, Hakhumyan G, Leroy C, Pashayan-Leroy Y and Sarkisyan D 2015 Complete hyperfine Paschen−Back regime at relatively small magnetic fields realized in potassium nano-cell *Europhys. Lett.* **110** 23001

[20] Arimondo E, Ciampini D and Rizzo C 2016 Chapter one-spectroscopy of natural and artificial atoms in magnetic fields *Advances in Atomic, Molecular, and Optical Physics* vol 65 ed E Arimondo, C C Lin and S F Yelin (New York: Academic) pp 1–66

[21] Whiting D J, Mathew R S, Keaveney J, Adams C S and Hughes I G 2018 Four-wave mixing in a non-degenerate four-level diamond configuration in the hyperfine Paschen−Back regime *J. Mod. Opt.* **65** 713

[22] Si R, Li W, Brage T and Hutton R 2020 Proposal for observation of transitions induced by external magnetic fields mixing in the lower states: with an example from Fe X *J. Phys. B: At. Mol. Opt. Phys.* **53** 095002

[23] Nyakang'o E O, Shylla D, Natarajan V and Pandey K 2020 Hyperfine measurement of the $6P_{1/2}$ state in $^{87}$Rb using double resonance on blue and IR transition *J. Phys. B: At. Mol. Opt. Phys.* **53** 095001

[24] Weller L, Kleinbach K S, Zentile M A, Knappe S, Hughes I G and Adams C S 2012 Optical isolator using an atomic vapor in the hyperfine Paschen−Back regime *Opt. Lett.* **37** 3405

[25] Abel R P, Krohn U, Siddons P, Hughes I G and Adams C S 2009 Faraday dichroic beam splitter for Raman light using an isotopically pure alkali-metal-vapor cell *Opt. Lett.* **34** 3071

[26] Kiefer W, Löw R, Wrachtrup J and Gerhardt I 2014 Na-Faraday rotation filtering: the optimal point *Sci. Rep.* **4** 6552

[27] Zentile M A, Whiting D J, Keaveney J, Adams C S and Hughes I G 2015 Atomic Faraday filter with equivalent noise bandwidth less than 1 GHz *Opt. Lett.* **40** 2000

[28] Zentile M A, Keaveney J, Mathew R S, Whiting D J, Adams C S and Hughes I G 2015 Optimization of atomic Faraday filters in the presence of homogeneous line broadening *J. Phys. B: At. Mol. Opt. Phys.* **48** 185001

[29] Rotondaro M D, Zhdanov B V and Knize R J 2015 Generalized treatment of magneto-optical transmission filters *J. Opt. Soc. Am.* B **32** 2507

[30] Keaveney J, Hamlyn W J, Adams C S and Hughes I G 2016 A single-mode external cavity diode laser using an intra-cavity atomic Faraday filter with short-term linewidth *Rev. Sci. Instrum.* **87** 095111

[31] Keaveney J, Wrathmall S A, Adams C S and Hughes I G 2018 Optimized ultra-narrow atomic bandpass filters via magneto-optic rotation in an unconstrained geometry *Opt. Lett.* **43** 4272

[32] Gomez M R, Hansen S B, Peterson K J, Bliss D E, Carlson A L, Lamppa D C, Schroen D G and Rochau G A 2014 Magnetic field measurements via visible spectroscopy on the Z machine *Rev. Sci. Instrum.* **85** 1

[33] Garn W B, Caird R S, Thomson D B and Fowler C M 1966 Technique for measuring megagauss magnetic fields using Zeeman effect *Rev. Sci. Instrum.* **37** 762

[34] Banasek J T, Engelbrecht J T, Pikuz S A, Shelkovenko T A and Hammer D A 2016 Measuring 10−20 T magnetic fields in single wire explosions using Zeeman splitting *Rev. Sci. Instrum.* **87** 103506

[35] Ciampini D, Battesti R, Rizzo C and Arimondo E 2017 Optical spectroscopy of a microsized Rb vapour sample in magnetic fields up to 58 tesla *Phys. Rev.* A **96** 052504

[36] George S, Bruyant N, Béard J, Scotto S, Arimondo E, Battesti R, Ciampini D and Rizzo C 2017 Pulsed high magnetic field measurement with a rubidium vapor sensor *Rev. Sci. Instrum.* **88** 073102

[37] Umfer C, Windholz L and Musso M 1992 Investigations of the sodium and lithium D-lines in strong magnetic fields *Z. Physik D Atoms, Mol. Clust.* **25** 23

[38] Windholz L 1985 Zeeman- and Paschen−Back-effect of the hyperfine structure of the sodium $D_1$-line *Z. Phys. Atom. Nucl.* **322** 203

[39] Windholz L and Musso M 1988 Zeeman- and Paschen−Back-effect of the hyperfine structure of the sodium $D_2$-line *Z. Physik D Atoms, Mol. Clust.* **8** 239

[40] Olsen B A, Patton B, Jau Y-Y and Happer W 2011 Optical pumping and spectroscopy of Cs vapor at high magnetic field *Phys. Rev.* A **84** 063410

[41] Weller L, Kleinbach K S, Zentile M A, Knappe S, Adams C S and Hughes I G 2012 Absolute absorption and dispersion of a rubidium vapour in the hyperfine Paschen−Back regime *J. Phys. B: At. Mol. Opt. Phys.* **45** 215005

[42] Zentile M A, Andrews R, Weller L, Knappe S, Adams C S and Hughes I G 2014 The hyperfine Paschen−Back Faraday effect *J. Phys. B: At. Mol. Opt. Phys.* **47** 075005

[43] Sargsyan A, Klinger E, Hakhumyan G, Tonoyan A, Papoyan A, Leroy C and Sarkisyan D 2017 Decoupling of hyperfine structure of Cs $D_1$ line in strong magnetic field studied by selective reflection from a nanocell *J. Opt. Soc. Am.* B **34** 776

[44] Siddons P, Adams C S, Ge C and Hughes I G 2008 Absolute absorption on rubidium D lines: comparison between theory and experiment *J. Phys. B: At. Mol. Opt. Phys.* **41** 155004

[45] Weller L, Bettles R J, Siddons P, Adams C S and Hughes I G 2011 Absolute absorption on the rubidium $D_1$ line including resonant dipole−dipole interactions *J. Phys. B: At. Mol. Opt. Phys.* **44** 195006

[46] Lange A J v, Straten P v d and Oosten D v 2020 Combined effect of non-linear optical and collisional processes on absorption

saturation in a dense rubidium vapour *J. Phys. B: At. Mol. Opt. Phys.* **53** 125402

[47] Siddons P, Bell N C, Cai Y, Adams C S and Hughes I G 2009 A gigahertz-bandwidth atomic probe based on the slow-light Faraday effect *Nat. Photon.* **3** 225

[48] Siddons P, Adams C S and Hughes I G 2009 Off-resonance absorption and dispersion in vapours of hot alkali-metal atoms *J. Phys. B: At. Mol. Opt. Phys.* **42** 175004

[49] Siddons P, Adams C S and Hughes I G 2010 Optical control of Faraday rotation in hot Rb vapor *Phys. Rev.* A **81** 043838

[50] Weller L, Dalton T, Siddons P, Adams C S and Hughes I G 2012 Measuring the Stokes parameters for light transmitted by a high-density rubidium vapour in large magnetic fields *J. Phys. B: At. Mol. Opt. Phys.* **45** 055001

[51] Whiting D J, Bimbard E, Keaveney J, Zentile M A, Adams C S and Hughes I G 2015 Electromagnetically induced absorption in a nondegenerate three-level ladder system *Opt. Lett.* **40** 4289

[52] Whiting D J, Keaveney J, Adams C S and Hughes I G 2016 Direct measurement of excited-state dipole matrix elements using electromagnetically induced transparency in the hyperfine Paschen–Back regime *Phys. Rev.* A **93** 043854

[53] Whiting D J, Šibalić N, Keaveney J, Adams C S and Hughes I G 2017 Single-photon interference due to motion in an atomic collective excitation *Phys. Rev. Lett.* **118** 253601

[54] Sargsyan A, Hakhumyan G, Leroy C, Pashayan-Leroy Y, Papoyan A, Sarkisyan D and Auzinsh M 2014 Hyperfine Paschen–Back regime in alkali metal atoms: consistency of two theoretical considerations and experiment *J. Opt. Soc. Am.* B **31** 1046

[55] Sargsyan A, Hakhumyan G, Tonoyan A, Petrov P A and Vartanyan T A 2015 Study of the Rb $D_2$-line splitting in a strong transverse magnetic field with Doppler-free spectroscopy in a nanocell *Opt. Spectrosc.* **119** 202

[56] Keaveney J, Ponciano-Ojeda F S, Rieche S M, Raine M J, Hampshire D P and Hughes I G 2019 Quantitative optical spectroscopy of $^{87}$Rb vapour in the Voigt geometry in DC magnetic fields up to 0.4 T *J. Phys. B: At. Mol. Opt. Phys.* **52** 055003

[57] Sargsyan A, Tonoyan A, Hakhumyan G, Papoyan A, Mariotti E and Sarkisyan D 2014 Giant modification of atomic transition probabilities induced by a magnetic field: forbidden transitions become predominant *Laser Phys. Lett.* **11** 055701

[58] Hakhumyan G, Leroy C, Mirzoyan R, Pashayan-Leroy Y and Sarkisyan D 2012 Study of 'forbidden' atomic transitions on $D_2$ line using Rb nano-cell placed in external magnetic field *Eur. Phys. J.* D **66** 119

[59] Zentile M A, Keaveney J, Weller L, Whiting D J, Adams C S and Hughes I G 2015 ElecSus: a program to calculate the electric susceptibility of an atomic ensemble *Comput. Phys. Commun.* **189** 162

[60] Keaveney J, Adams C S and Hughes I G 2018 ElecSus: extension to arbitrary geometry magneto-optics *Comput. Phys. Commun.* **224** 311

[61] Smith D A and Hughes I G 2004 The role of hyperfine pumping in multilevel systems exhibiting saturated absorption *Am. J. Phys.* **72** 631

[62] Sherlock B E and Hughes I G 2009 How weak is a weak probe in laser spectroscopy? *Am. J. Phys.* **77** 111

[63] Adams C S and Hughes I G 2019 *Optics F2f: From Fourier to Fresnel* (Oxford: Oxford University Press)

[64] Schaefer B, Collett E, Smyth R, Barrett D and Fraher B 2007 Measuring the Stokes polarization parameters *Am. J. Phys.* **75** 163

[65] Truong G-W, Anstie J D, May E F, Stace T M and Luiten A N 2012 Absolute absorption line-shape measurements at the shot-noise limit *Phys. Rev.* A **86** 030501

[66] Trénec G, Volondat W, Cugat O and Vigué J 2011 Permanent magnets for Faraday rotators inspired by the design of the magic sphere *Appl. Opt.* **50** 4788

[67] Keaveney J 2014 *Collective Atom–Light Interactions in Dense Atomic Vapours* (*Springer Theses*) (Berlin: Springer)

[68] Weller L 2013 Absolute absorption and dispersion in a thermal Rb vapour at high densities and high magnetic fields *PhD Thesis* Durham University

[69] Sargsyan A, Sarkisyan D and Papoyan A 2006 Dark-line atomic resonances in a submicron-thin Rb vapor layer *Phys. Rev.* A **73** 1

[70] Jahier E, Guéna J, Jacquier P, Lintz M, Papoyan A V and Bouchiat M A 2000 Temperature-tunable sapphire windows for reflection loss-free operation of vapor cells *Appl. Phys. B: Lasers Opt.* **71** 561

[71] Steffen A, Alt W, Genske M, Meschede D, Robens C and Alberti A 2013 Note: *In situ* measurement of vacuum window birefringence by atomic spectroscopy *Rev. Sci. Instrum.* **84** 126103

[72] Knappe S, Gerginov V, Schwindt P D D, Shah V, Robinson H G, Hollberg L and Kitching J 2005 Atomic vapor cells for chip-scale atomic clocks with improved long-term frequency stability *Opt. Lett.* **30** 2351

[73] Hughes I G and Hase T P A 2010 *Measurements and Their Uncertainties: A Practical Guide to Modern Error Analysis* (Oxford: Oxford University Press)

[74] Rotondaro M D and Perram G P 1997 Collisional broadening and shift of the rubidium $D_1$ and $D_2$ lines ($5^2S_{12} \rightarrow 5^2P_{12}$, $5^2P_{32}$) by rare gases, $H_2$, $D_2$, $N_2$, $CH_4$ and $CF_4$ *J. Quant. Spectrosc. Radiat. Transfer* **57** 497

[75] Ejlli A, Della Valle F, Gastaldi U, Messineo G, Pengo R, Ruoso G and Zavattini G 2020 The PVLAS experiment: a 25 year effort to measure vacuum magnetic birefringence (arXiv:2005.12913 [hep-ex, physics:physics])

[76] Carr D L, Spong N L R, Hughes I G and Adams C S 2020 Measuring the Faraday effect in olive oil using permanent magnets and Malus' law *Eur. J. Phys.* **41** 025301

[77] Ojed F S Ponciano 2020 Absorption spectroscopy and Stokes polarimetry in a 87Rb vapour in the Voigt geometry with a 1.5 T external magnetic field [Dataset] https://collections.durham.ac.uk/files/r1kk91fk595